

The low-mass YSO CB230-A: investigating the protostar and its jet with NIR spectroscopy and Spitzer observations.

F. Massi¹, C. Codella², J. Brand³, L. Di Fabrizio⁴, and J.G.A. Wouterloot⁵

¹ INAF-Osservatorio Astrofisico di Arcetri, Largo E. Fermi 5, 50125 Firenze, Italy

² INAF, Istituto di Radioastronomia, Sezione di Firenze, Largo E. Fermi 5, 50125 Firenze, Italy

³ INAF, Istituto di Radioastronomia, Via P. Gobetti 101, 40129 Bologna, Italy

⁴ INAF, Telescopio Nazionale Galileo, 38700 Santa Cruz de la Palma, Spain

⁵ Joint Astronomy Centre, 660 N. A'ohoku Place, University Park, Hilo, 96720 HI, USA

Received date; accepted date

ABSTRACT

Context. To investigate the earliest phases of star formation and study how newly-born stars interact with the surrounding medium, we performed a line and continuum survey at NIR and mm-wavelengths of a sample of relatively isolated Bok globules.

Aims. We present a follow-up observational program of a star-forming site in the globule CB230. From narrow-band continuum observations of this site, we had discovered a bright [FeII] jet, which originates in the low-mass YSO CB230-A. We aim to investigate the physical properties of the region from where the jet is launched.

Methods. Our analysis was carried out using low-resolution NIR spectra acquired with the camera NICS at the TNG telescope, with *JH* and *HK* grisms and a 1 arcsec-wide slit. These observational data were complemented with infrared photometric data from the Spitzer space telescope archive.

Results. The relevant physical properties of CB230-A were constrained by SED fitting of fluxes from the NIR to the mm. The YSO spectrum exhibits a significant number of atomic and molecular emission lines and absorption features. The characteristics of this spectrum suggest that we are observing a region in the close vicinity of CB230-A, i. e. its photosphere and/or an active accretion disk. The spectra of the knots in the jet contain a large number of emission lines, including a rich set of [FeII] lines. Emission due to H₂ and [FeII] are not spatially correlated, confirming that [FeII] and H₂ are excited by different mechanisms, in agreement with the models where [FeII] traces dissociative J-shocks and molecular hydrogen traces slower C-shocks. By using intensity ratios involving density-sensitive [FeII] lines, we estimated the electron densities along the jet to be $6 \times 10^3 - 1 \times 10^4 \text{ cm}^{-3}$. This indicates either high density post-shock regions of ionised gas or regions with a high degree of ionisation.

Conclusions. By combining the present data with previously obtained maps at NIR- and mm-wavelengths, the emerging scenario is that CB230-A is a Class 0/I YSO driving an atomic jet that is observed to be almost monopolar probably due to its inclination to the plane of the sky and the resulting higher extinction of its red side. This primary jet appears to be sufficiently energetic to open the cavity visible in the NIR images and drive the large-scale molecular outflow observed at mm-wavelengths. **CB230-A was revealed to be a good location to test the innermost structure of accreting low-mass protostars.**

Key words. Stars: formation – Stars: winds, outflows – ISM: jets and outflows – ISM: molecules – ISM: individual objects: CB230

1. Introduction

High-velocity jets driven by collimated winds generated by Young Stellar Objects (YSOs) interact strongly with the surrounding medium, cleaning up the high-density material hosting the star-forming process. Jets are also thought to remove angular momentum from the accreting matter allowing lower angular momentum gas to carry on the build-up process of a new star. In addition, when they travel into the ambient cloud, jets create shocks that heat (up to thousands of K) and compress the gas, and drive bipolar molecular outflows on larger spatial scales containing colder (10-100 K) swept-up material. As a consequence, the study of the acceleration and collimation of jets is fundamental to understanding star formation.

Some of the most accessible places to survey jets are represented by Bok globules (Bok & Reilly 1947), which are relatively isolated molecular clouds mainly associated with low-mass star formation (e.g. Huard et al. 1999 and references therein). The globule CB230 (Clemens & Barvainis 1988) is a

good example, given the simultaneous presence of almost all the ingredients expected in a typical star formation scenario: YSOs, a hot atomic jet, and a colder molecular outflow. One of the YSOs in the cloud (hereafter called CB230-A) was detected in the Near-Infrared (NIR) as well as at sub-millimetre wavelengths (Yun & Clemens 1992, 1994a; Launhardt & Henning 1997; Huard et al. 1999; Young et al. 2003). It is also associated with a bipolar outflow, observed in CO (Yun & Clemens 1994b). Using N₂H⁺ observations, Chen et al. (2007) found a clear velocity gradient across the molecular core of $\sim 8.8 \text{ km s}^{-1} \text{ pc}^{-1}$, in the same direction as the line connecting CB230-A with a source $\sim 10''$ east. This latter source close to CB230-A was detected at $7 \mu\text{m}$ with ISOCAM and coincides with a possibly double NIR source (CB230-B,C; see Fig. 1).

The distance to CB230 was discussed by Launhardt & Henning (1997), who placed it at 450 pc. This was derived by associating CB230 with a larger molecular cloud complex (Cepheus Flare), based on their respective radial velocities. The authors estimated that the given distance is accurate to within 30%. Kun (1998) discussed the distance to the Cepheus Flare

molecular cloud complex and for L1177 (the dark cloud hosting CB230) quotes a distance in the range 300–560 pc, where the lower value is the kinematic distance and the higher one is the distance to the nearby (but probably unrelated) reflection nebula vdB141. Although kinematic distances lower than 1 kpc are of doubtful reliability, the lowest value agrees with the distance (300 ± 30 pc) derived for the dark clouds in the area by studying the cumulative distribution of stellar distance moduli (Wolf diagram). Young et al. (2006) assumed $d = 288$ pc taking this value from Straizys et al. (1992), who derived the distance to a group of dark clouds (close to L1177, but not including it) using photometry of 79 stars. In particular, L1167/L1174 were found to lie at $d = 288 \pm 25$ pc, in agreement with the lower value indicated by Kun (1998) for L1177. In summary, it seems that $d = 450$ pc ($\pm 30\%$) is a robust determination and 288 pc may be assumed as a safe lower limit.

CB230-A is classified as a Class 0/Class I source (e. g., Froebrich 2005). Estimates of the bolometric luminosity, based on the IRAS fluxes, range from $7.7 L_{\odot}$ (Froebrich 2005) to $12 L_{\odot}$ (Launhardt & Henning 1997), both for a distance of 450 pc, i. e. the distance we adopt. From our sub-mm observations with SCUBA (Brand et al. 2008), we derive a gas mass of $3.4 M_{\odot}$, which agrees within a factor of 2 with the mass estimated by Launhardt (2001) from observations at 1.3 mm with the IRAM 30-m. Launhardt (2001) also found a disk of mass $\sim 0.1 M_{\odot}$ around the protostar, based on observations at 1mm continuum with the Owens Valley Radio Interferometer. By using three different evolutionary models, Froebrich (2005) derived an age in the range 1.7×10^4 – 2.2×10^5 yrs and a final stellar mass in the range 0.3 – $0.9 M_{\odot}$.

In the framework of our ongoing multi-frequency study of star formation in Bok globules (Massi et al. 2004; Codella et al. 2006), we carried out narrow-band NIR observations centred on the $1.644 \mu\text{m}$ [FeII] and $2.122 \mu\text{m}$ H_2 lines. As a result, we detected a bright [FeII] jet in CB230, which (i) originates in CB230-A and extends for ~ 0.02 pc, (ii) is directed along the same direction as the molecular outflows axis (N-S), and (iii) is defined by two knots (called k1 and k2) superimposed on fainter elongated emission observed also in H_2 (Massi et al. 2004). Figure 1 illustrates this by displaying an overlay of the [FeII] image and the CO(3–2) bipolar outflow as mapped by Brand et al. (2008). These [FeII] and H_2 NIR lines are particularly useful, since [FeII] emission traces fast and dissociative J-shocks, which should outline the inner jet-channel, whereas H_2 emission is expected to trace slower C-shocks that probably originate in bow-shocks, probing the region of interaction between the jet and the ambient gas. The CB230 NIR maps therefore support a complex scenario, which, to be confirmed, requires further [FeII] and H_2 spectroscopic NIR observations; these data were obtained and enabled us to constrain the physical properties of the gas (such as extinction and excitation temperature) in the region where the jet interacts with the surrounding dense gas close to its origin, i. e. close to the central system, which consists of a protostar and, presumably, an accretion disk.

2. Observations and data reduction

The spectroscopic observations were carried out on the night of August 3, 2004, with the NIR camera NICS at the Telescopio Nazionale Galileo (TNG) at La Palma. We obtained spectra through the grisms *JH* (1.15 – $1.75 \mu\text{m}$) and *HK* (1.40 – $2.50 \mu\text{m}$), using a $1''$ -wide slit. This provided a spectral resolution of $R \sim 500$. The slit was aligned along the [FeII] jet defined by the k1 and k2 knots, hence encompassing also the driving source

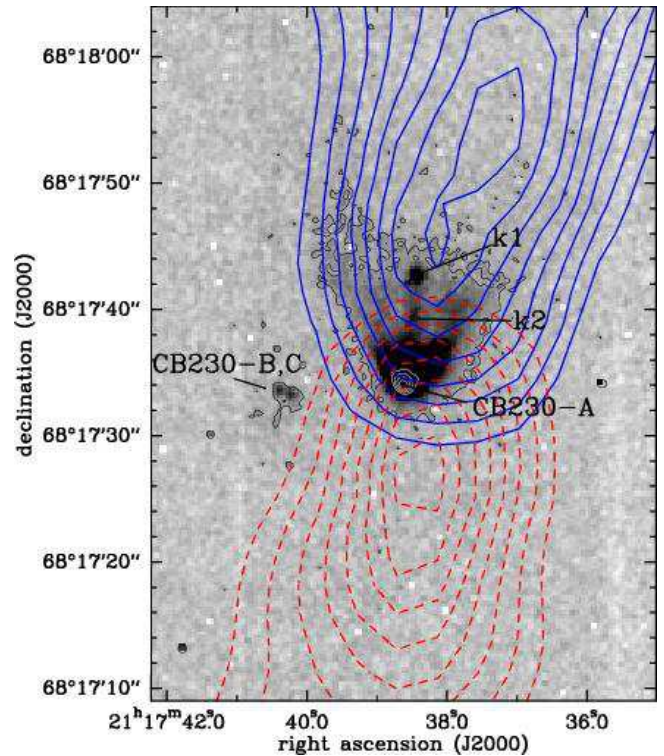


Fig. 1. Continuum-subtracted [FeII] map (grey scale; Massi et al. 2004) of CB230: the white contours mark the brightest emission indicating the YSO CB230-A. The label CB230-B,C mark two NIR objects, that could make a triple system with CB230-A. The labels k1 and k2 indicate the two [FeII] knots defining the jet. Also visible is an extended diffuse component showing the cavity opened by the YSO mass ejection. In contours, the CO(3–2) integrated emission of the blue (continuous) and red (dashed) lobes of the molecular outflow driven by CB230-A (Brand et al. 2008; JCMT-data). The integration intervals are from -6 to $+1.37$ km s^{-1} (blue lobe) and from $+4.68$ to $+14$ km s^{-1} (red lobe). Contours range from 3 to 20 K km s^{-1} in steps of 1 K km s^{-1} . The blue lobe extends for $\sim 120''$, the red one is roughly half as long.

(the YSO). Six spectra of the target were obtained through the grism *JH* in an ABBAAB set of cycles (i. e. integrating when the source is in a position A on the detector, then nodding the telescope along the slit projection on the sky to move the source to a different position B on the detector, integrating again and reversing the cycle, etc.). The integration time for each spectrum was 900 s. Two spectra were taken through the grism *HK* in a single AB cycle, with integration times of 600 s each. The star HIP97033 (spectral type GO V) was observed in between the *JH*- and the *HK*-cycles on the source, by acquiring four spectra in an ABBA cycle with 2 s of integration each, through both the *JH*- and the *HK*-grism. Other spectra of this star and of HIP108772 (spectral type O9 V) were taken at the beginning of the night, but they could not be used to correct the target spectra for telluric absorption because they were observed at least 5 hours before the target. However, they were used to obtain the intrinsic spectrum of HIP97033 and perform other tests on the telluric correction. The weather conditions did not remain stable and observations of the target could be carried out only in the late night due to clouds.

Data reduction was done using IRAF¹. All frames were flat-field corrected by using spectra of a halogen lamp, following the prescriptions given on the TNG web page, i. e. the halogen frames were normalised row-by-row by dividing by a low-degree polynomial fit of the background. All frames were wavelength-calibrated and rectified by using reference spectra of an Argon lamp. Then, each pair of subsequent frames (i. e. the A and B exposures in AB- or BA-cycles) were subtracted to remove background emission and other biases. Since a single frame (i. e. A or B in AB- or BA-cycles) is an image where the source spectrum appears as a row of bright pixels, after subtraction a frame is obtained that contains two spectra of the source, one positive and one negative with respect to the average background level. By careful examination of the [FeII] images in Massi et al. (2004), we estimated the extent of the two emission knots and the YSO in the spatial direction, and extracted their spectra from each subtracted frame (two per frame). Two spectra of HIP97033 per subtracted frame were also extracted.

Using the solar spectrum as an input, a synthetic spectrum was constructed (following Maiolino et al. 1996) that represented an arbitrarily-scaled version of the intrinsic spectrum of HIP97033 (assuming a radial velocity of -21.6 km s^{-1} and a rotational velocity of 10 km s^{-1} , as listed in the SIMBAD database). For all extracted spectra of HIP97033, the wavelength calibration was then further refined by aligning the intrinsic absorption lines in each stellar spectrum with the corresponding ones in the synthetic (reference) spectrum. This is required because moving the telescope produces small shifts in the wavelength scale of each frame (i. e. there exists a shift between the wavelength scale in the Ar-lamp frames and that in each of the source frames). Finally, all other spectra were further wavelength-corrected (to minimize this instrumental effect) by shifting their wavelength scale to align their atmospheric absorption lines with those in the final stellar spectra. This correction translated into shifts of $\sim 10^{-3} \mu\text{m}$ (i. e. $\sim 10 \text{ \AA}$, independent of wavelength) both for the telluric standard and the targets. All spectra of a given source were then coadded to obtain the highest signal-to-noise ratio. The atmospheric transmission was corrected for as explained in Maiolino et al. (1996), i. e., by dividing the spectra of the knots and the YSO by that of the telluric standard and then multiplying them by the synthetic intrinsic spectrum of the star obtained from the solar spectrum.

2.1. Flux calibration

We first dereddened the spectra over the entire wavelength range by adopting the reddening law of Rieke & Lebofsky (1985). We tentatively derived A_V from [FeII] line ratios (see Sect. 3.1; the uncertainties affecting the obtained values are further discussed in Sect. 4.3). Once A_V was known, the reddening correction was obtained by dividing each spectrum by a curve proportional to the extinction as a function of the wavelength. Then, the dereddened spectra were flux-calibrated according to the following prescriptions. For the knots (i. e. Figs. 2 and 3), we required that the total flux of the [FeII] line at $1.645 \mu\text{m}$ equalled the narrow-band photometric determinations of Massi et al. (2004).

For CB230-A (i. e. Fig. 4), each of the J , H , and K segments of the dereddened YSO spectrum was first multiplied by the total transmission of the 2MASS system (atmosphere excluded);

the derived flux densities were then integrated over each of the J , H , and K passbands and divided by the integral of the total 2MASS transmission over the corresponding passband. The resulting mean flux densities were eventually set to be equal to the flux densities derived from the 2MASS magnitudes of the YSO (2MASS21173862+6817340, $J = 14.085 \pm 0.062$, $H = 11.712$, $K = 10.487$) after being dereddened using the same A_V used to deredden the entire spectrum. We then obtained two conversion factors (counts to flux density) from JH (one from J and one from H) and two conversion factors from HK (one from H and one from K).

Obviously, the two conversion factors for each of the two YSO spectra (i. e. JH and HK) should coincide. For the HK spectrum, the conversion factors obtained from H and K agree to within a few percent, whereas for the JH spectrum, those obtained from J and H differ by $\sim 30\%$. The two different calibration factors within JH probably reflect errors in the photometry due to the presence of diffuse emission towards the YSO and possible time-variability slightly affecting the SED (spectra and 2MASS data were obviously not taken simultaneously).

However, the calibrated YSO spectra have different continuum emission slopes within the overlapping H interval, with differences in flux of up to $\sim 20\%$. The same problem is found when calibrating with the integrated flux in the [FeII] line at $1.645 \mu\text{m}$, which produces differences in the slope of the underlying continuum towards the knots of up to $\sim 30\%$. Inaccuracies in the telluric correction are discussed in Appendix A and do not appear to affect the spectra significantly. The most likely cause is the intense, extended emission around the source, which could have prevented an accurate placement of the slit on the central source.

2.2. Spitzer observations

Spitzer observations of CB230 were taken from the Spitzer public archive. They consisted of IRAC images at the four wavelengths (3.6 , 4.5 , 5.8 , and $8 \mu\text{m}$) and MIPS images at 24 and $70 \mu\text{m}$. The observations were part of the GTO program 124, “IRAC and MIPS Imaging and IRS Spectroscopy of Pre and Post Main Sequence Stellar Systems” (Principal Investigator G. Gehrz). Overviews of IRAC and MIPS were given by Fazio et al. (2004) and Rieke et al. (2004), respectively.

We retrieved all post-BCD (Basic Calibrated Data) images, which were produced by the pipeline version S14.0.0 (IRAC), S16.1.0 (MIPS at $24 \mu\text{m}$), and S16.0.1 (MIPS at $70 \mu\text{m}$). All MIPS data were obtained in the photometric small field modes (fine scale at $70 \mu\text{m}$). After checking all images for possible problems as described in the instrument Data Handbooks², we decided not to repeat the reduction steps starting from the BCD images, and photometry was carried out on the post-BCD images.

CB230-A and CB230-B(C) are resolved in the IRAC and MIPS $24 \mu\text{m}$ images, but blended in the MIPS $70 \mu\text{m}$ images. CB230-B and CB230-C are unresolved even in the IRAC images, so they were considered to be a single source (hereafter, CB230-B+C). Aperture photometry of both CB230-A and CB230-B+C was performed using DAOPHOT in IRAF. We selected aperture radii of 2 pixels ($\sim 2''$ [IRAC], $3''$ [MIPS $24 \mu\text{m}$], and $35''$ [MIPS $70 \mu\text{m}$]). The background contribution was measured within annuli with inner radius of 2 pixels and width of 4 pixels (IRAC), inner radius of $6''$ and width of $7''$ (MIPS at $24 \mu\text{m}$), and inner radius of $39''$ and width of $26''$ (MIPS at

¹ IRAF is distributed by the National Optical Astronomy Observatories, which are operated by the Association of Universities for Research in Astronomy, Inc., under cooperative agreement with the National Science Foundation.

² <http://ssc.spitzer.caltech.edu/>

Table 1. Spitzer magnitudes of CB230-A and CB230-B+C.

Band (μm)	CB230-A (mag)	CB230-B+C (mag)
3.6	9.101 ± 0.004	12.62 ± 0.04
4.5	8.537 ± 0.006	12.06 ± 0.04
5.8	8.033 ± 0.006	11.49 ± 0.06
8	7.88 ± 0.01	10.21 ± 0.01
24	2.847 ± 0.004	4.48 ± 0.02
70 ^a	-3.75 ± 0.07	

^a CB230-A and CB230-B+C are spatially unresolved in this band and appear as a single source.

24 μm). We adopted aperture corrections given on the Spitzer web page³, for the used apertures and sky annuli. In the case of the MIPS 24 μm image, the aperture photometry for each of the two sources was performed after subtraction of the other source by PSF fitting. The photometric uncertainties were computed as described by Reach et al. (2005) and Gordon et al. (2007). We note that due to flux density nonlinearities, aperture photometry is expected to underestimate the MIPS 70 μm flux, probably by $\sim 20\%$ (Gordon et al. 2007). The fluxes were converted into magnitudes in the IRAC (Reach et al. 2005) and MIPS (see the MIPS handbook) systems and are listed in Table 1.

3. Results

3.1. Emission lines

The complete *JHK* spectra of the knots k1 and k2 and of the YSO CB230-A are shown in Figs. 2, 3, and 4, respectively. The spectra were dereddened using the visual extinctions derived from [FeII] line ratios (see below). In Table 2, we list fluxes and identification for all the detected emission lines at the three positions (k1, k2, and CB230-A). We note that we considered detections to be only those lines with an S/N ≥ 3 and with line widths of comparable or larger than the instrumental resolution. Table 2 also contains a number of tentative detections (also labelled in Figs. 2, 3, and 4) with a S/N ≈ 2 . The three spectra show a rich set of [FeII] emission lines, as well as the H₂ emission line at 2.12 μm : in particular, the knot k1 exhibits a large number of bright emission features. These confirm the presence of H₂ emission and unveil the structure of the [FeII] line-emission, providing improvements to the interpretations of narrow-band filter data by Massi et al. (2004).

3.2. YSO spectral shape

All spectra show an underlying continuum emission, whose shape (before correction for extinction) is similar in all directions, i. e. towards both the YSO and the knots. However, in the YSO spectrum, the continuum emission is more intense and exhibits several emission and absorption features. Longward of 1.3 μm , the beginning of an absorption band can be seen in all spectra, which can be identified as being due to water (see Sect. 4.4). A check of the spectra uncorrected for telluric absorption confirms that this band is intrinsic and not a telluric feature. The continuum emission from the knots most likely originates from the scattering of radiation by dust grains. The ubiquitous presence of this water absorption band indicates that the illumination source is the YSO. Another absorption band clearly visible longward of 2.29 μm , is easily identifiable as the CO(2,0)

band. This clearly indicates that the central star photosphere and/or the innermost region of the circumstellar disk are being observed through a cavity produced by the outflow.

4. The YSO

4.1. YSO classification

The classification of both CB230-A and CB230-B+C can be checked by using Spitzer data to derive their spectral indices between 2 and 24 μm . Assuming that $\lambda F_\lambda \propto \lambda^\alpha$, we estimated that $\alpha \sim 2$ (CB230-A) and $\alpha \sim 2.4$ (CB230-B+C) from the 2MASS *K* fluxes and MIPS 24 μm fluxes. Both objects can be then identified to be Class I sources.

The Mid-Infrared (MIR) colours also, derived from the magnitudes given in Table 1, can provide information about the evolutionary stage of the two objects. In a [3.6]–[4.5] versus [5.8]–[8.0] colour-colour plot (CCP), both lie outside the “disk domain” (i. e. the plot region dominated by Class II sources) from Allen et al. (2004). CB230-A colours would be consistent both with those of a reddened photosphere (although for an A_V of at least 40 mag), as well as with those of an accreting protostar (“stage” I source, according to the classification proposed by Robitaille et al. 2006). CB230-B+C colours are located in a region occupied mainly by both stage II sources (in practise, they are mostly Class II sources) and stage I sources. The information from a [3.6]–[5.8] versus [8.0]–[24.0] CCP is more helpful. Both CB230-A and CB230-B+C colours are consistent with those of stage I sources or heavily reddened ($A_V > 20 - 30$ mag) stage II sources.

4.2. YSO SED

As a further step towards an understanding of the evolutionary stage and physical properties of CB230-A, we used a more complete set of observational data spanning the wavelength interval from the NIR to the mm. Model SEDs could then be fitted to the data and the relevant physical properties of the YSO derived. The source fluxes at different wavelengths, and the effective or estimated aperture radii for which they were measured, are listed in Table 3.

By integrating the SED, we found that the ratio of the luminosity for wavelengths longer than 350 μm to the bolometric luminosity is ~ 0.01 , which would lead to its classification as a Class 0 source (André et al. 2000). Given also its properties in the NIR to MIR, we can therefore understand its classification as a transition Class 0/Class I source.

To fit the SED of CB230-A, we used the online fitting tool by Robitaille et al. (2007). This exploits a grid of 20000 protostar models for which the radiation transfer has been solved, accounting for the central star, envelope and disk and including cavities and scattering. A wide range of physical conditions in each component is covered (Robitaille et al. 2007). We constrained the distance to be in the range 280–600 pc (see Sect. 1). All models (i. e., 16) within a range $\chi^2 - \chi^2_{\text{best}} < 250$ (per datapoint) are shown in Fig. 5, where $\chi^2_{\text{best}} = 233.47$ is the value (per datapoint) from the best fit. Clearly, these appear to fit the SED reasonably on a by-eye basis. The high values of χ^2 are due partly to having underestimated the uncertainties (in most bands, we adopted the photometric errors only). In fact, we found that by increasing the errors in the IRAC and 1.3 mm fluxes to 10 %, the χ^2 of the best-fit model decreased to 315 (i. e. 20 per datapoint), whereas the range of physical parameters is not significantly changed. Nevertheless, we also checked that none of

³ <http://ssc.spitzer.caltech.edu/>

Table 2. Emission lines observed towards the knots k1 and k2 and the YSO CB230-A: detections and tentative detections. The values between brackets are the measured r.m.s.

Transition	λ^b (μm)	k1 ^a	k2 ^a	CB230-A ^a
		F (10^{-15} erg cm ⁻² s ⁻¹)		
[FeII] a ⁴ D _{7/2} – a ⁶ D _{9/2}	1.2567	78.6(2.0)	125.8(4.8)	38.7(2.3)
[FeII] a ⁴ D _{1/2} – a ⁶ D _{1/2}	1.2704 ^c	9.5(2.1) ^c	–	7.9(1.6) ^c
[FeII] a ⁴ D _{3/2} – a ⁶ D _{3/2}	1.2788	10.8(2.0)	–	14.2(1.6)
[FeII] a ⁴ D _{5/2} – a ⁶ D _{5/2}	1.2943	11.1(2.9)	–	7.7(2.0)
[FeII] a ⁴ D _{7/2} – a ⁶ D _{7/2}	1.3206	22.7(2.4)	21.6(5.1)	16.0(1.6)
[FeII] a ⁴ D _{5/2} – a ⁶ D _{3/2}	1.3278	7.6(2.3)	–	–
[FeII] a ² I _{11/2} – b ² H _{9/2}	1.5246	5.0(1.3)	10.7(5.2) ^d	–
[FeII] a ⁴ D _{5/2} – a ⁴ F _{9/2}	1.5335	12.3(2.0)	11.2(5.2) ^d	21.5(5.9)
[FeII] a ⁴ D _{3/2} – a ⁴ F _{7/2}	1.5995	5.7(1.7)	–	–
[FeII] a ⁴ D _{7/2} – a ⁴ F _{9/2}	1.6436	58.4(1.1)	60.8(2.8)	46.5(6.1)
[FeII] a ⁴ D _{1/2} – a ⁴ F _{5/2}	1.6638	5.2(1.7)	–	–
[FeII] a ⁴ D _{5/2} – a ⁴ F _{7/2}	1.6769 ^e	4.7(1.1)	–	10.9(6.3) ^e
HI 11-4	1.6811 ^e	–	–	15.7(6.3) ^e
H ₂ 1–0 S(1)	2.122	11.7(3.1)	15.4(2.5)	38.3(2.9)
HI 7-4	2.1661	–	–	10.8(2.9)

^a The *JHK* spectra have been dereddened using the visual extinctions derived from the [FeII] 1.645/1.321 line ratio (see Tab. 6). ^b The wavelengths of the [FeII] lines are taken from the NIST atomic spectra database. ^c Blended with a telluric line. ^d S/N \approx 2: tentative detection. ^e The HI and [FeII] lines at 1.68 μm are blended.

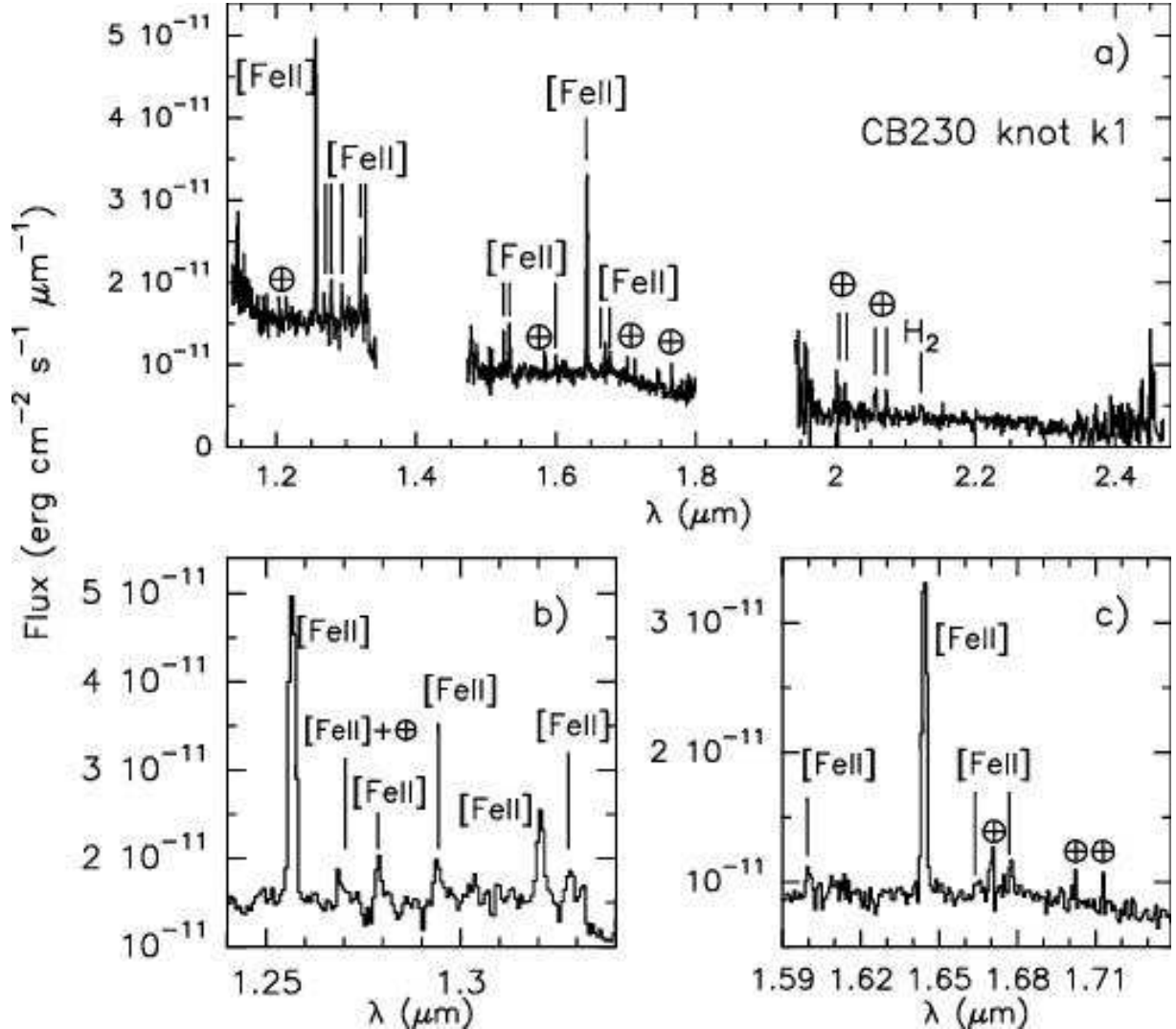


Fig. 2. (a) NIR (*JHK*) dereddened spectra ($A_V = 14$ mag) obtained with the TNG towards the [FeII] knot k1 (see Fig. 1). Telluric lines have been marked, too. (b) and (c) Zoom-in on the spectral regions around the bright [FeII] emission lines at 1.26 and 1.64 μm , where several other weaker [FeII] lines have been detected. Table 2 provides the complete list of detections and tentative detections of emission lines.

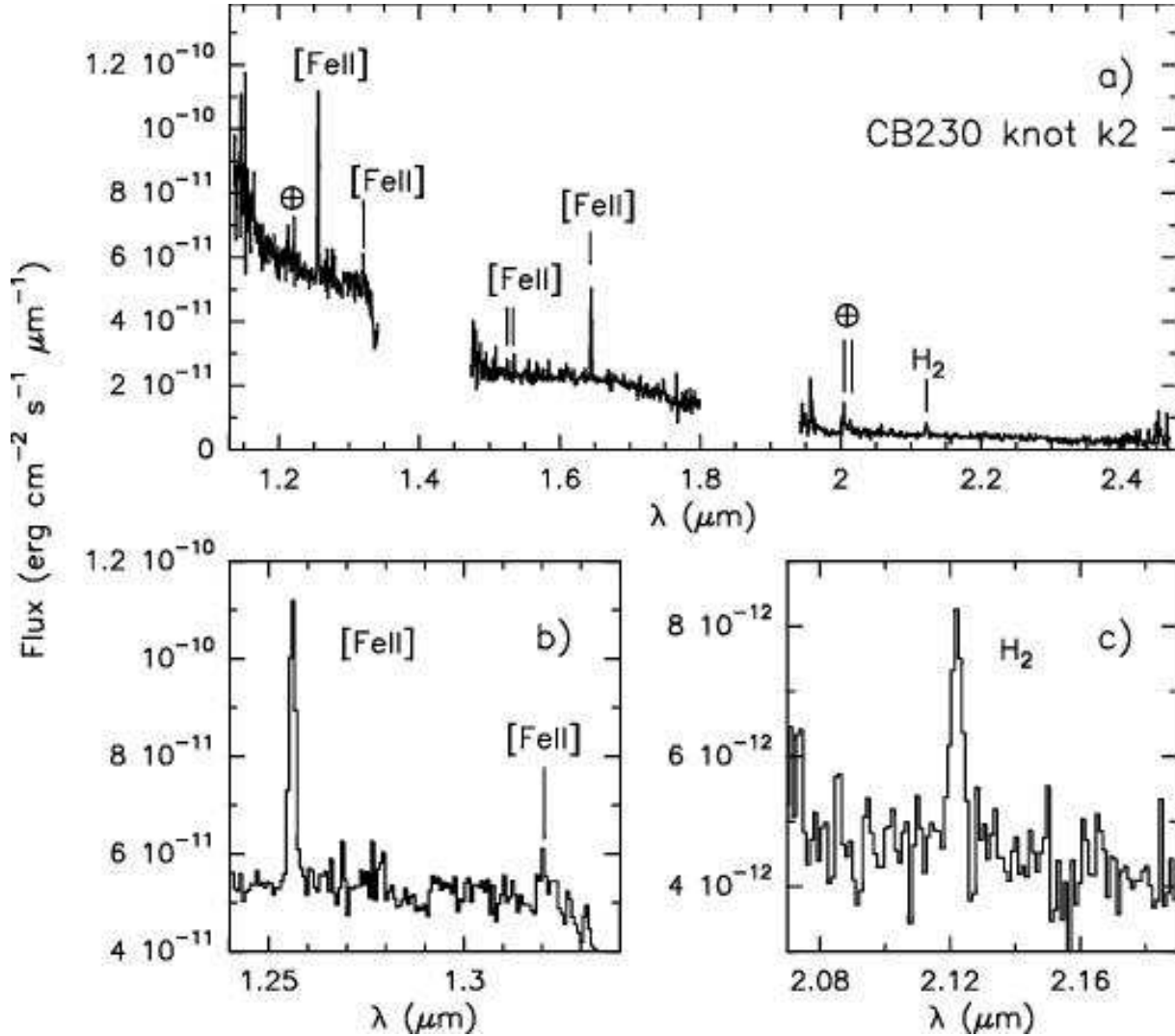


Fig. 3. (a) NIR (*JHK*) dereddened spectra ($A_v = 18.5$ mag) obtained with the TNG telescope towards the [FeII] knot k2 (see Fig. 1). Telluric lines have been marked, too. (b) and (c) Zoom-in on the spectral regions where the bright [FeII] emission line at $1.26 \mu\text{m}$ and the H_2 emission $2.12 \mu\text{m}$ line have been detected. Table 2 provides the complete list of detections and tentative detections of emission lines.

the grid models is able to fit equally well the NIR-MIR and FIR-submm parts of the SED. In Table 4, we list the most relevant physical parameters for the best-fit model and their range for the remaining 15 models within the above χ^2 interval.

Clearly, a picture emerges of a very young low-mass ($\sim 0.5 M_\odot$) central protostar with a high accretion rate. This agrees with its previous classification as a transition Class 0/Class I source. The age and mass determination also agree with the compilation by Froebrich (2005). Its inclination with respect to the line-of-sight is not large, as expected since only one side of a cavity is visible in the NIR. A circumstellar disk is present with a mass $\sim 0.01 M_\odot$. This is in accord with a disk mass $\sim 0.1 M_\odot$ inferred by Launhardt (2001) based on interferometric mm observations, since Robitaille et al. (2007) checked that by using their fitting tool, the agreement between fitted disk masses and other disk mass determinations (when these are available), is always good to within one order of magnitude. However, we note that some of the best-fit models exhibit disk masses much smaller than $\sim 0.01 M_\odot$, although the accretion rate is always quite high. This implies that even the available MIR data are un-

able to constrain strongly the circumstellar disk physical properties.

Another problem is that all models appear to be underluminous with respect to the estimated bolometric luminosity. This partly arises because of the range of fitting distances; after scaling all total luminosities instead to a distance of 450 pc (at which the reported bolometric luminosity estimates are derived) we achieve closer agreement between measurement and predictions of bolometric luminosity (see Table 4). Nevertheless, the total luminosity remains underestimated. This is clear from Fig. 5, where all model SEDs are always below the datapoints in the FIR-to-mm range. This reflects the intrinsic inadequacies of the model grid in describing the physical properties of CB230-A already noted. These models do not account for example for the luminosity generated by the envelope accretion (Robitaille et al. 2006), which may in fact be important in this case.

We also attempted to fit the SED of CB230-B+C with the same constraints as for CB230-A (but obviously without datapoints in the FIR to mm range). The best-fit model has $\chi^2_{\text{best}} = 17.84$ (per datapoint) and its relevant physical parameters are listed in Table 5, along with those of the models (36) with

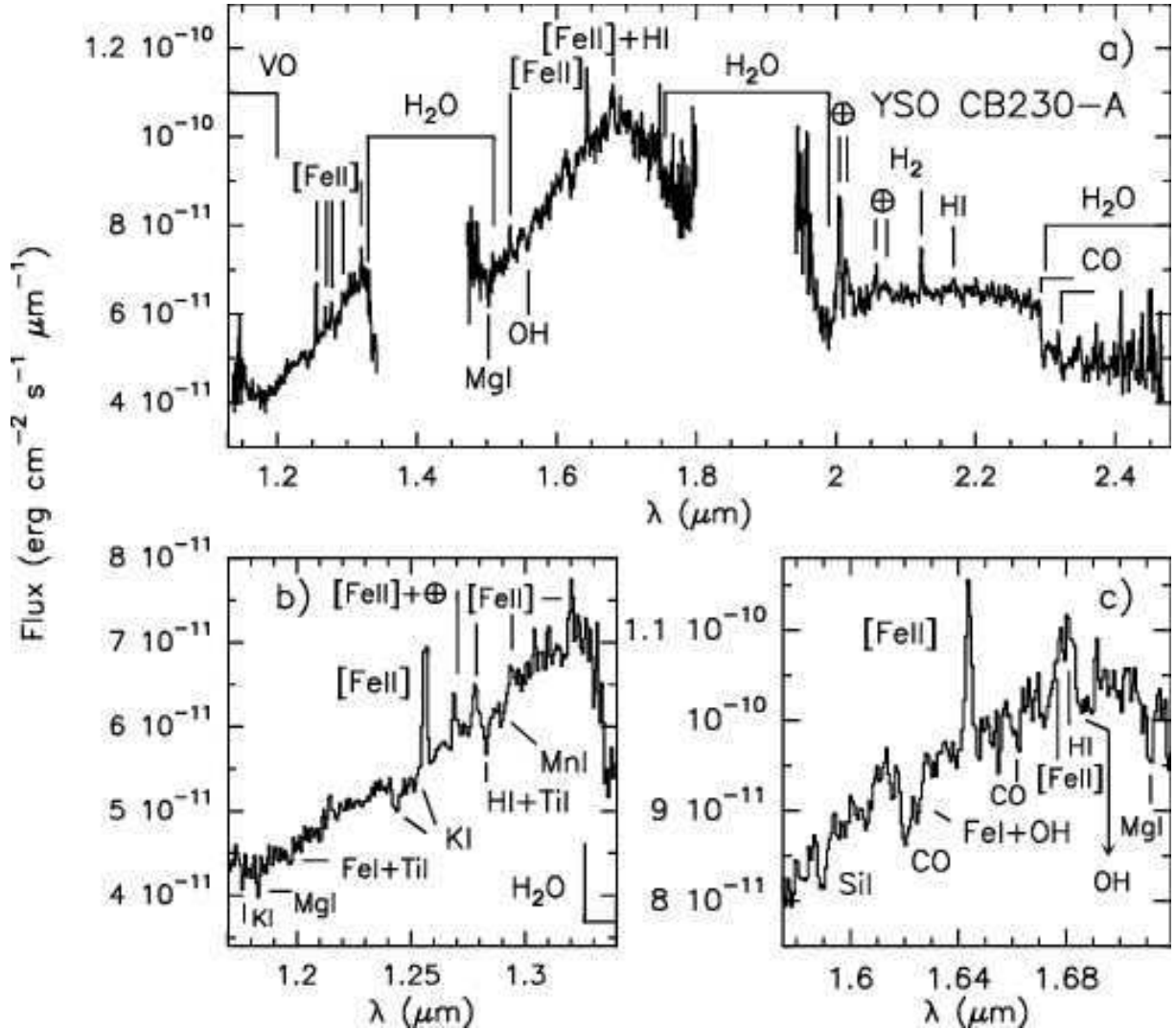


Fig. 4. (a) NIR (*JHK*) dereddened spectra ($A_V = 8.4$ mag) acquired by the TNG towards the YSO CB230-A, which drives the jet/outflow system (see Fig. 1). Telluric lines are indicated. Tables 2 and 7 provide the complete list of detections and tentative detections of emission and absorption lines, respectively. We note the absorption band at wavelengths less than $1.2 \mu\text{m}$, possibly due to VO, the three H₂O absorption bands around 1.4 , 1.9 and $2.4 \mu\text{m}$, as well as the two CO absorption bands at 2.29 and $2.32 \mu\text{m}$. Panels (b) and (c) present a zoom-in view of the spectral regions where the bright [FeII] emission lines at 1.26 and $1.64 \mu\text{m}$ are detected. Note that for the sake of clarity all the absorption features (detections and tentative detections), except for MgI at $1.50 \mu\text{m}$ and OH at $1.56 \mu\text{m}$, are labelled only in panels (b) and (c).

$\chi^2 - \chi_{\text{best}}^2 < 30$ (per datapoint). Unfortunately, the lack of measurements in the FIR and submm ranges prevents us from constraining strongly many of the physical parameters. The best-fit model is that of a relatively evolved $M \sim 1.5 M_{\odot}$ protostar with an edge-on disk that is no longer accreting. This can probably be discarded, based on the interferometric mm measurements by Launhardt (2001) that set an upper limit of $0.006 M_{\odot}$ to the disk mass of CB230-B+C. However, there still remains a combination of Class I and Class II sources with central masses in the range $\sim 0.1 - 1.5 M_{\odot}$ that are able to fit the SED of CB230-B+C. Given the possible binary nature of this source, more data are also required to arrive at a more definite identification. This source will not be discussed further in the following.

4.3. Scattering and extinction in the NIR

In principle, the NIR spectrum of the YSO provides a powerful means to constrain further its total photospheric absorption. The

most intense emission lines are due to three [FeII] transitions at $1.257 \mu\text{m}$, $1.321 \mu\text{m}$, and $1.645 \mu\text{m}$. Since these [FeII] lines correspond to the same upper energy level (see Table 2), the line ratios $1.645/1.321 \mu\text{m}$ and $1.645/1.257 \mu\text{m}$ can be used to estimate the extinction towards the [FeII]-emitting regions. The three lines are within the observed wavelength range of grism *JH*; determination of these ratios is therefore straightforward and no intercalibration that exploits partly overlapping spectral intervals is required. The fluxes were computed from Gaussian fits to the lines and the noise was measured in small adjoining spectral intervals. Finally, the extinction was derived towards the YSO and the two knots following Nisini et al. (2005b), and is listed in Table 6. The quoted uncertainties were obtained by propagating the noise. Clearly, there appear to be some discrepancies in the extinction estimated from the two line ratios. Nisini et al. (2005b) pointed out that these discrepancies are generally found when deriving the extinction from the two line ratios, such that the $1.645/1.257$ -ratio appears to overestimate A_V . They rec-

Table 3. Fluxes of CB230-A used for SED fitting. Those for CB230-B+C are also listed when the two (unresolved) sources are not blended with CB230-A.

Band (μm)	CB230-A (mJy)	CB230-B+C (mJy)	Aperture radius ($''$)
1.235 ^a	3.702 ± 0.211	< 0.748	4
1.662 ^a	21.159	1.128 ± 0.124	4
2.159 ^a	42.57	3.893 ± 0.218	4
3.6 ^b	64.3 ± 0.2	2.51 ± 0.08	2.4
4.5 ^b	69.1 ± 0.4	2.70 ± 0.09	2.4
5.8 ^b	70.4 ± 0.4	2.9 ± 0.2	2.4
8 ^b	45.4 ± 0.4	5.27 ± 0.07	2.4
12 ^c	< 250		67
24 ^d	521 ± 2	116 ± 2	3
25 ^c	680 ± 70		67
60 ^c	11750 ± 700		95
70 ^d	24566 ± 1500		35
100 ^c	33530 ± 2000		134
450 ^e	10430		50
850 ^e	2330		20
1300 ^f	221 ± 5		6

^a 2MASS catalogue; ^b Spitzer/IRAC, this work; ^c IRAS PSC; ^d Spitzer/MIPS, this work; ^e SCUBA, Brand et al. (2008); ^f IRAM 30-m, Launhardt & Henning (1997);

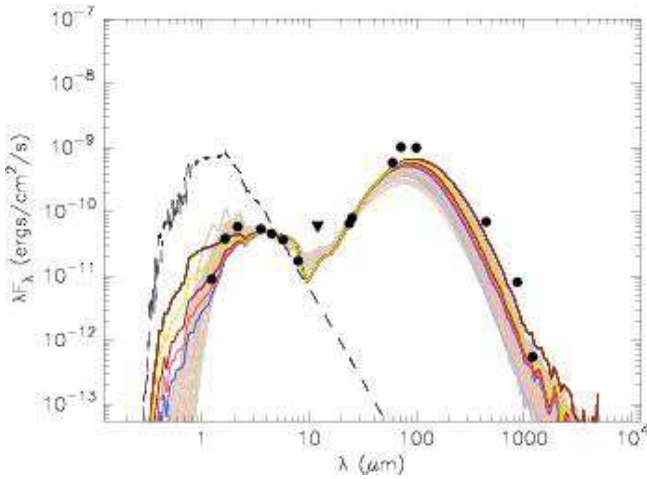


Fig. 5. Model SEDs (full colour lines in the electronic edition) that best fit the fluxes of CB230-A (full dots; the full triangle marks an upper limit), within a range $\chi^2 - \chi_{\text{best}}^2 < 250$ (per datapoint).

The dashed line marks the stellar photosphere of the best-fit model.

commend using the 1.645/1.321-ratio, which they found provides results that are more consistent with other independent determinations. However, in our case it is evident that the two values of A_V are always equal within the uncertainties, that appear then dominated by the line signal-to-noise ratio, rather than by the uncertainty in the transition probabilities suggested by Nisini et al. (2005b). However, in Appendix B we propose an alternative explanation for the disagreement between the extinction values obtained from the two line ratios: the 1.257 μm line intensity can be underestimated because of unaccounted-for telluric absorption. In the following, we follow the prescription of Nisini et al. (2005b) and use extinctions derived from the 1.645/1.321-ratio.

The error in line ratios due to inaccurate correction of the atmospheric absorption (and large-scale differences in system sensitivity) can be estimated to be $\sim 10\%$, according to the discussion in Appendix A. This would cause the extinction $A_{1.644 \mu\text{m}}$ to

Table 4. Relevant physical parameters of the protostellar model that most accurately reproduces the SED of CB230-A and their ranges for the remaining 15 models in the interval $\chi^2 - \chi_{\text{best}}^2 < 250$ (per datapoint).

Physical parameter	Best fit	Range
χ^2	3735.51	3804.37–7668.63
Interstellar extinction A_V (mag)	0.00	3.79–18.02
Distance (pc)	295	282–513
Age (yr)	5.2×10^4	2.7×10^4 – 10^5
Central mass (M_\odot)	0.4	0.15–0.5
Star radius (R_\odot)	4	3.4–4.9
Star temperature (K)	3600	2908–3759
Accretion rate ($M_\odot \text{ yr}^{-1}$)	10^{-4}	10^{-4} – 10^{-6}
Envelope outer radius (AU)	5784	1968–7757
Cavity aperture angle (deg)	23	21–29
Disk mass (M_\odot)	0.03	7.7×10^{-5} –0.05
Disk inner radius (AU)	0.1	0.06–0.3
Disk accretion rate ($10^{-8} M_\odot \text{ yr}^{-1}$)	2.3	0.0077–3.6
Inclination to the line of sight (deg)	31.8	18.2–31.8
YSO inner extinction A'_V ^a (mag)	48.09	0.09–37.33
Total photospheric extinction $A_V + A'_V$ (mag)	48.09	6.5–42
Total system luminosity (L_\odot)	2.585	0.846–4.287
Total system luminosity scaled to $d = 450$ pc (L_\odot)	6	2.2–5.7

^a I. e., the extinction from the outer edge of the circumstellar envelope to the stellar surface along the line of sight.

Table 5. Relevant physical parameters of the protostellar model that most accurately reproduces the SED of CB230-B+C and their ranges for the remaining 36 models in the interval $\chi^2 - \chi_{\text{best}}^2 < 30$ (per datapoint).

Physical parameter	Best fit	Range
χ^2	142.72	242.36–382.14
Interstellar extinction A_V (mag)	15.04	5.26–24.96
Distance (pc)	525	316–602
Age (yr)	1.9×10^6	5.2×10^3 – 10^7
Central mass (M_\odot)	1.4	0.10–1.59
Star radius (R_\odot)	2.4	1.6–4.3
Star temperature (K)	4540	2559–5655
Accretion rate ($M_\odot \text{ yr}^{-1}$)	0	0 – 4.5×10^{-5}
Disk mass (M_\odot)	0.037	2.7×10^{-5} –0.029
Disk inner radius (AU)	36	0.044–16.6
Disk accretion rate ($10^{-7} M_\odot \text{ yr}^{-1}$)	4.0	0.00019–1.69
Inclination to the line of sight (deg)	87.13	18.2–87.13
YSO inner extinction A'_V ^a (mag)	459.4	4×10^{-5} –182
Total system luminosity (L_\odot)	8.230	0.33–6.91

^a I. e., the extinction from the outer edge of the circumstellar envelope to the stellar surface along the line of sight.

be over- or under-estimated by ~ 0.2 mag, which translates into $\Delta A_V \sim 1.2$ mag. Comparing this with the values listed in Table 6 shows that in all cases but one (i. e. k1), the uncertainty in the reddening due to the signal-to-noise ratio of the single lines is larger or of the order of that intrinsic to the telluric correction.

Finally, it is worth noting that from our SCUBA maps in the sub-mm continuum (Brand et al. 2008), we expect a total extinction (i. e., over the entire width of the clump) $A_V = 37$ mag, or $A_V = 18.5$ mag for objects in the centre of the clump. The values inferred from the [FeII] line ratios towards the knots k1 and k2 are equal or less than that. It is also noteworthy that the upper limit to the total photospheric extinction ($A_V + A'_V$, where A_V is the extinction up to the outer edge of the circumstellar envelope

Table 6. Visual extinction derived from [FeII] line ratios.

Source	A_V	
	1.645/1.321 (mag)	1.645/1.257 (mag)
k1	14.0(1.1)	14.0(0.2)
k2	18.5(3.2)	14.5(3.4)
CB230-A	8.4(3.5)	12.3(1.3)

and A'_V that from there to the photosphere), listed in Table 4, is of the same order as that inferred from the sub-mm emission.

Nevertheless, the extinction derived for the YSO spectrum, although within the range of total photospheric extinction ($A_V + A'_V$) listed in Table 4 and obtained from the SED fits, is lower than 18.5 mag. This, as well as the lowest values of $A_V + A'_V$ obtained, is consistent with a picture in which the jet has removed part of the gas and dust from the line of sight, although we would expect a lower extinction from the knots, as well (see below). If dereddened by $A_V = 8.4$ mag, the intrinsic colour of the YSO is $J-K = 2.2$, which would be consistent with NIR colours of main sequence dwarf stars of type later than L2. Their photospheric temperatures are lower than the temperatures obtained from the SED fits (see again Table 4), but their spectral type would be consistent with the presence of water and CO absorption in the spectrum. However, to derive the photospheric extinction from the [FeII] lines we must assume that these lines originate close to the central protostar. Instead, there are indications that other effects must also be taken into account. First of all, many models of those that describe the SED most accurately exhibit a higher total photospheric extinction. Secondly, the continuum appears redder than is usual for spectra of late-M and early-L giants, and spectra of dwarf stars with strong water and CO absorption bands (see Sect. 4.4). Thirdly, the extinction *decreases* from the knots to the YSO: we would however expect the YSO to be more embedded than the knots, since the knots are emerging from the cavity. And finally, once they are dereddened, the J flux density of knots k1 and k2 is higher than that of the YSO at the shortest wavelengths of band J : this cannot however be true if the continuum radiation from the knots is produced by dust scattering of infrared emission from the YSO. In this respect, the extinction derived for the YSO from the 1.645/1.257 μm ratio would enable a more consistent picture, although we remark again that in the literature this ratio is found to overestimate extinction systematically.

In particular, the following effects may alter the intrinsic [FeII] line ratios:

1. the extinction derived from the [FeII] line ratios may differ from the actual reddening of the continuum spectrum of the YSO (and the knots) because these lines might trace a different environment (the densest part of the jet), which is only seen in projection towards the YSO (i. e. matter between this environment and the YSO could not be accounted for in the extinction derivation);
2. the observed [FeII] line ratios might be affected by absorption lines in the background photospheric spectrum being almost coincident with some of the emission lines and, then, lowering their measured flux;
3. part or all of the observed radiation from the YSO might have been scattered by the dust before being extinguished.

With reference to item 3, we tried to infer the effects of scattering by adopting the results of Whitney et al. (1997). Using a two-dimensional Monte Carlo radiative transfer code, they modelled NIR scattering in cavities, swept out by jets, of the emission

from a protostar (surrounded by a circumstellar disk) embedded in an infalling, rotating cloud with a density profile $\sim r^{-2}$. For a number of models, they indicated the ratios R_λ of the scattered flux to the intrinsic source flux ($R_\lambda = F_{s,\lambda}/F_{0,\lambda}$) in the J, H, K , and L bands. We fitted a $\lambda^{-\alpha}$ function to their average values for R_λ ($R_J = 0.0013$, $R_H = 0.0071$, and $R_K = 0.018$) and used this function to correct the spectra for scattering approximately. At first we assumed that the observed radiation was first scattered and then extinguished; we therefore modified the intrinsic line ratios of [FeII] by accounting for the derived $\lambda^{-\alpha}$ “scattering” function. These new line ratios then replaced the intrinsic values in the formula that defines A_V as a function of the observed [FeII] line ratios. This yielded negative values for A_V , showing either that the used set of R_λ is unrepresentative of the source-cavity system, or that only the continuum was scattered, but the [FeII] emission was only extinguished.

Next, we assumed that the observed radiation was scattered within the cavity but not subsequently extinguished. This would be the case if the jet had almost completely cleared the cavity and this was inclined towards the observer. Using the same models that were later used by Whitney et al. (1997), Whitney & Hartmann (1993) found that if the angle between the cavity axis and the line-of-sight is less than 66° , the image of the cavity no longer looks bipolar because of the extinction of its red side. In the case of CB230, since the cavity is not bipolar (see Fig. 1), it must be inclined towards the observer, which is also suggested by the far smaller red lobe of the CO outflow. It is therefore plausible that scattered light from the YSO is little extinguished in its path to the observer. Remarkably, if we use the $\lambda^{-\alpha}$ function instead of the reddening law and correct the spectrum only for scattering, we obtain a bluer continuum (see Fig. 6) and the [FeII] 1.645/1.321 and 1.645/1.257 line ratios are only 7% and 14% less than the intrinsic ones, respectively. Then, the adopted scattering correction would naturally yield the intrinsic [FeII] line ratios, suggesting that the observed YSO spectrum is also consistent with pure scattered emission from the innermost regions of the globule, emerging through the cavity.

Figure 6 shows examples of the YSO spectrum after correction for scattering only, after correction for dust extinction of $A_V = 12.3$ mag, and after correction for $A_V = 8.4$ mag.

In summary, our scattering model is oversimplified. Without more detailed modelling of CB230-A, it is difficult to disentangle the effects of scattering and extinction. We therefore adopt the conservative approach of correcting the YSO spectrum only for a reddening of $A_V = 8.4$ mag, derived from the [FeII] line ratios. This choice does not affect the measured absorption-line equivalent widths, or the emission-line fluxes, which remain good estimates provided that they are produced along the jet, but far from the protostar-disk system.

4.4. Absorption features towards CB230-A: a tentative spectral identification

The presence of absorption features in the YSO spectrum, if produced by the photosphere, would allow us to constrain the physical parameters of the central protostar more reliably. Spectral identifications of Class I sources have been successfully carried out in the NIR by a number of authors (see e. g. Nisini et al. 2005a, Doppmann et al. 2005, and references therein), but always using medium or high spectral resolution data. These authors found ubiquitous CO overtone absorption bands, and a number of absorption lines, due to the “cold” photospheres of the central protostars. However, CB230-A is the first instance

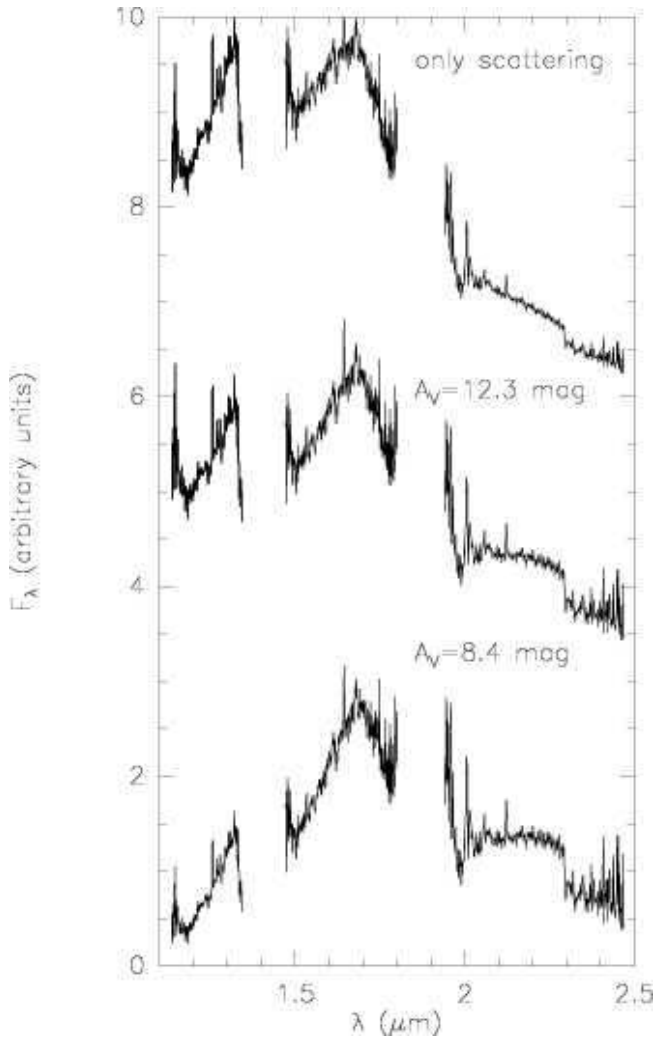


Fig. 6. From top to bottom: YSO spectrum corrected only for scattering (see Sect. 4.3), corrected for $A_V = 12.3$ mag and corrected for $A_V = 8.4$ mag. All spectra have been normalised to the peak of the emission and shifted along the y-axis.

of a Class I source exhibiting both water absorption bands and other absorption features at low spectral resolution.

In Fig. 4, the spectrum towards the YSO is shown after dereddening by $A_V = 8.4$ mag, i. e. the value derived from the [FeII] 1.645/1.321 line ratio. The continuum emission peaks in the H band and there are prominent absorption bands longward of $1.3 \mu\text{m}$ (H_2O) and $2.29 \mu\text{m}$ (first and second CO overtone). Other absorption lines (also labelled in Fig. 4) were found in the spectrum; we identified them by comparison with spectra of late-M and early-L type photospheres. Both detections ($S/N \geq 3$) and tentative detections of absorption features are listed in Table 7, following the spectral catalogues of Wallace et al. (2000; MK standards in the J -band), Meyer et al. (1998; MK standards in the H -band), Lancon & Rocca-Volmerange (1992) and Dallier et al. (1996; both papers discuss NIR spectra of O- to M-stars of luminosity classes I to V), Reid et al. (2001) and Cushing et al. (2005; both about M- and L-dwarfs).

Unfortunately, as can be seen in Table 7, most equivalent widths are only few sigma and the K -part of the spectrum is of too low signal-to-noise to enable reliable detection of any absorption lines. Nevertheless, a few lines are discernible in the J and H spectra. Furthermore, a few absorption features were

Table 7. Atomic absorption lines and molecular bands observed towards the YSO CB230-A: detections and tentative detections

Atom/Molecule	λ^a (μm)	EW^b (\AA)
KI	1.1778	0.67(0.27) ^c
MgI	1.1828	0.89(0.27)
FeI, TiI	1.1974	0.64(0.36) ^c
KI	1.2437	1.76(0.29)
KI	1.2529 ^d	0.59(0.29) ^c
HI (Pa β), TiI	1.2827	1.25(0.31)
MnI	1.2905	0.70(0.31) ^c
MgI	1.5028	2.63(0.62)
OH(2-0)P(11)	1.5575	1.08(0.28)
SiI ^e	1.5894	1.97(0.32)
CO(6,3)	1.6187	3.7(0.4)
FeI, OH(2-0)P(15) ^f	1.6250 ^f	1.4(0.4)
CO(8,5)	1.6617	0.94(0.37) ^c
OH(2-0)P(18)	1.6877	0.72(0.28) ^c
MgI	1.7113	1.39(0.32)
CO(2,0)	2.2935	12.00(0.83)

^a All wavelengths of the atomic transitions are taken from Cushing et al. (2005), except for that of MgI at $1.18 \mu\text{m}$, taken from the NIST atomic spectra database. The OH wavelengths are from Maillard et al. (1976), while those of CO are from Dallier et al. (1996) and Meyer et al. (1998). ^b The equivalent widths were measured in the spectra after dereddening by using the visual extinctions derived from the [FeII] 1.645/1.321 line ratio (see Tab. 6); however, this should have little effect on the found values. ^c $S/N \sim 2$: tentative detection. ^d Blended with the [FeII] emission line at $1.2567 \mu\text{m}$ (see Tab. 2). ^e Possible contamination due to the OH(2-0)P(13) band at $1.5902 \mu\text{m}$. ^f The wavelengths of FeI and OH(2-0)P(15) are 1.6236 and $1.6265 \mu\text{m}$, respectively. Here we report the observed wavelength.

identified beyond any doubt: the H_2O bands at $1.3\text{--}1.5$, $1.75\text{--}2.05$, and $2.3\text{--}3.2 \mu\text{m}$ and the CO(2,0), CO(3,1), and CO(6,3) overtone bands longward of 2.29 , 2.32 , and $1.62 \mu\text{m}$, respectively.

Given the low spectral resolution and low signal-to-noise of the YSO spectrum, and the uncertainty in the spectral slopes, we decided not to perform a spectral identification by using fits of template spectra. We instead used the identified features to check their consistency with the photospheric temperatures derived by the SED fit. These were compared with known features of late-type dwarfs (class V) and giant (class III) stars: we must consider the latter stellar types in particular because the radius of the central protostar is expected to be larger, corresponding to a low surface gravity, which affects gravity-sensitive lines. Furthermore, the presence of a circumstellar disk causes veiling of the absorption lines, which must be taken into account. We also applied the diagnostics for late-type star identification proposed by Meyer et al. (1998) in the H -band and by Wallace et al. (2000) in the J -band, and derived the values of a few spectral indices based on the water and CO bands, and Na lines, in late-M to L dwarfs, as devised by Reid et al. (2001), McLean et al. (2003), and Allers et al. (2007).

In Fig. 7, the spectrum of CB230-A (for two different extinction and scattering corrections) is compared with low-resolution spectra of M3V, M8.5V, M4III, and M6IIIe stars. In spite of the uncertainties in the slopes, the H_2O and CO bands ensure that the YSO spectrum resembles that of late M (or even early L dwarfs), or late M giants. Conversely, the absorption lines identified in the J band are more typical of either early M dwarfs or M giants. The clearest detections are lines from KI, which are in fact gravity-sensitive (McGovern et al. 2004). The CO(6,3) band is also a signature of giant (luminosity class III) stars. However,

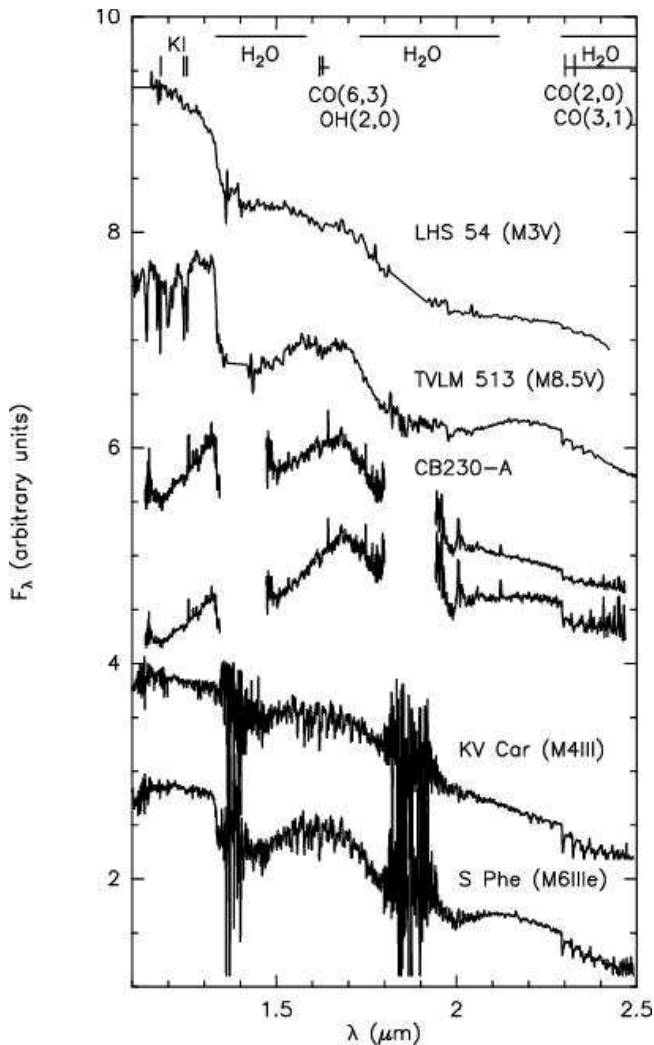


Fig. 7. NIR spectra of CB230-A (corrected for $A_V = 8.4$ mag, upper, and for scattering only, lower) compared with low-resolution spectra of LHS 54 (an M3V star, from Leggett et al. 2000), TVLM 513-46546 (an M8.5V star, from Leggett et al. 2001), KV Car (an M4III star, from Lancon et al. 2000) and S Phe (an M6IIIe star, from Lancon et al. 2000). The main lines and spectral features identified in the spectrum of CB230-A are labelled. Each spectrum has been normalised to its flux at $1.7 \mu\text{m}$.

the measured equivalent widths of all CO band-heads seem more typical of K rather than M stars (see also Origlia et al. 1993 for a list of typical values). These disagreements probably reflect both a lower gravity with respect to dwarf stars and veiling by the NIR emission of the circumstellar disk. Other indications of lower gravity come from the possible detection of the A–X 0–1 VO band around $1.18 \mu\text{m}$ and the measured $1.14 \mu\text{m}$ Na-index (as defined by Allers et al. 2007). In summary, the YSO spectrum can be identified as later than M2 (with M2 a conservative limit) with some indications of a lower gravity than in dwarf stars.

4.5. Cold photosphere and/or active accretion disk

Since the mass of the protostar is expected to be $< 0.5 M_\odot$ (see Table 4), which agrees with the mass determinations ($< 0.1 M_\odot$) of the circumstellar disk, clearly most of the bolometric luminosity must be generated by the accretion. According to the

T_{eff} scale adopted by Meyer et al. (1998) and tabulated in their Table 2, T_{eff} is ~ 3530 K for a luminosity class V (~ 3710 K for a luminosity class III) at the upper end of the inferred spectral type interval (M2). This is within the range of central temperatures derived from the SED fits (see Table 4). However, the protostar models of the SED-fitting tool adopt the pms tracks of Siess et al. (2000) for the central star, which do not account for accretion. It would therefore be meaningful to compare our observations with models of accreting protostars. In this respect, Palla & Stahler (1991; 1992; 1993) follow the growth of an accreting protostar up to intermediate masses. Then, the evolution of the bolometric luminosity (including the fraction provided by accretion), T_{eff} , and protostellar mass can be evaluated along their birthline.

From our CO maps obtained at the JCMT antenna (Brand et al. 2008), we estimate an outflowing mass rate of $\sim 6 \times 10^{-7} M_\odot \text{ yr}^{-1}$. Consequently, following theoretical models of star formation (e.g. Shu et al. 2000), we expect an accretion rate 10–100 times higher, i.e. around $10^{-5} M_\odot \text{ yr}^{-1}$. This is also within the range derived from the SED fits (see Table 4). For such a value, Palla & Stahler (1993) found that a bolometric luminosity of $\sim 7.7 L_\odot$ is produced by a protostar of $\sim 1.5 M_\odot$ with $T_{\text{eff}} \sim 4467$ K, i. e. a more massive central object hotter than envisaged so far. We note that if we use $d = 288$ pc, i. e. the lower limit of the distance determination (Sect. 1), we find more precise agreement, although still marginal, obtaining $T_{\text{eff}} \approx 3980$ K and $M \sim 0.6 M_\odot$.

Another way to improve agreement between the observations and the model is to increase the accretion rate, which would produce a higher bolometric luminosity for a given mass and, as a consequence, T_{eff} could be lowered. However, if we assumed an accretion rate of $10^{-4} M_\odot \text{ yr}^{-1}$ then a protostar of $< 1 M_\odot$ would need less than 10^4 yrs to be assembled. But this would be less than our estimated outflow dynamical age ($\sim 3 \times 10^4$ yrs at $d = 450$ pc, assuming an inclination with respect to the line-of-sight of $i \sim 45^\circ$). If the dynamical age can be considered to be a lower limit to the age of the driving source, this rules out an accretion rate of more than $10^{-4} M_\odot \text{ yr}^{-1}$. This again agrees with the upper limit of the accretion rate derived by the SED fits.

Wuchterl & Tscharnuter (2003) presented evolutionary tracks of protostars following the collapse of Bonnor-Ebert spheres. Their tracks showed that $T_{\text{eff}} \sim 3000$ K and bolometric luminosities of $\sim 7.7 L_\odot$ can be obtained for central protostars of $\sim 0.5 M_\odot$ and < 0.3 Myr old. By using these tracks, we therefore obtain a far closer agreement with our observations. Nevertheless, according to this model, the protostar would have already accreted $\sim 90\%$ of the initial clump mass, which is inconsistent with the high current envelope mass that we have measured ($\sim 3.4 M_\odot$).

One other possibility to be considered is that a few spectral features (namely the strong absorption bands of CO and H₂O) are *not* photospheric in origin, but are produced in an active accretion disk. The NIR spectra of FU Ori stars exhibit strong absorption bands of water and first and second overtones of CO, in contrast with their optical identification as F–G supergiants (Mould et al. 1978). This was attributed to the NIR part of FU Ori spectra being generated by an accretion disk (Calvet et al. 1991a). Calvet et al. (1991b) showed that for central stars with $T_{\text{eff}} < 6000$ K, mass accretion rates of $> 10^{-7} M_\odot \text{ yr}^{-1}$ are able to turn the CO bands into absorption. Even if the mass of the protostar were $1 M_\odot$, it could have been accumulated in less than 10^7 yr with an accretion rate of only $> 10^{-7} M_\odot \text{ yr}^{-1}$. These values lie at the upper end of the acceptable ranges of both age and mass. It is therefore possible that at least some of the features in

the YSO NIR spectrum are produced in an active accretion disk rather than in a protostellar photosphere.

Clearly, these issues will be resolved by future high-resolution high-sensitivity NIR spectral observations, which will enable a more robust spectral classification to be achieved and allow us to recognise the kinematical signature of a disk in the line profiles, irrespective of reddening and scattering corrections.

4.6. Spectral indicators of the accretion rate

Muzerolle et al. (1998) found a tight correlation between the emission luminosity of Br γ and the accretion luminosity in a sample of classical T-Tauri stars. We can use their Eq. 2 and the line luminosity estimated from the flux listed in Tab. 2 (assuming $d = 450$ pc) to derive an accretion luminosity of $\sim 0.15 L_{\odot}$. This would be consistent with “low” accretion rates ($\sim 10^{-7} M_{\odot} \text{ yr}^{-1}$) and central masses ($\sim 0.1 M_{\odot}$), but in total disagreement with the observed “high” bolometric luminosity, which in this case should be produced mostly by accretion. By raising the central mass to obtain higher stellar luminosities, we must however resort to the active disk scenario to produce the CO bands in absorption, which would again disagree with the low accretion luminosity derived from the Br γ flux. Part of the discrepancy may be due to the likely underestimate of the extinction (or the neglect of scattering) already discussed. For instance, an underestimate in A_V of 3 mag would increase the derived accretion luminosity to $\sim 4.5 L_{\odot}$, in far closer agreement with the estimated bolometric luminosity. However, this would assume that the Muzerolle et al. (1998) relation is applicable in addition to less evolved YSOs.

5. The outflow

5.1. Physical properties of the jet from the NIR spectra

The extinction of the knots was derived in Sect. 4.3 using the ratios of the intense emission lines due to three [FeII] transitions at 1.257 μm , 1.321 μm , and 1.645 μm . The values obtained are listed in Table 6 and we adopted those derived from the 1.645/1.321 μm ratio. All the other observed [FeII] lines (see Table 2 and Figs. 2 and 3) are associated with similar excitation levels ($\sim 11000\text{--}12000$ K) and therefore cannot be used to derive temperature estimates (e.g. Nisini et al. 2005b). On the other hand, these [FeII] lines have different critical densities ranging between 10^4 and 10^5 cm^{-3} . Following the model developed by Nisini et al. (2005b), it is possible to derive an estimate of the electron density (n_e) by using intensity ratios involving the brightest transitions which are density-sensitive (i. e. 1.645/1.600, 1.645/1.533, and 1.645/1.677). For the CB230-A position, we obtain $1.645/1.600 \geq 2.2$, $1.645/1.533 = 2.2$, and $1.645/1.677 = 4.3$, which are consistent with $n_e \geq 10^5 \text{ cm}^{-3}$. In other words, the density towards the YSO is higher than the critical density of the [FeII] lines, which are therefore expected to be thermalised. For the knot k1, we derived $1.645/1.600 = 10.3$, $1.645/1.533 = 4.3$, and $1.645/1.677 = 12.5$, which correspond to electron densities in the $6 \times 10^3 - 1 \times 10^4 \text{ cm}^{-3}$ range. Finally, the weaker k2 spectrum indicates $1.645/1.600 \geq 7.5$, $1.645/1.533 = 5.4$, and $1.645/1.677 \geq 7.5$, again suggesting densities of around 10^4 cm^{-3} . Our measurements confirm the findings of Nisini et al. (2005b) in HH-flows associated with three SFRs, i. e. that the NIR [FeII] emission lines trace either high density post-shock portions of the ionised gas or regions of a high degree of ionisation and then a high electron density. Unfortunately, to derive the hydrogen ionisation fraction x_e , following the procedure intro-

duced by Bacciotti & Eisloffel (1999), we would need measurements of oxygen and nitrogen lines in the optical and to assume that these lines trace the same material that emits the NIR [FeII] lines. To derive a rough estimate of the total hydrogen density, $n_H = n_e/x_e$, we can only assume that the ionisation fraction is equal to the typical value measured in a number of jets (e.g. Podio et al. 2006, and references therein), $x_e = 0.03\text{--}0.6$. If this is also valid in the CB230 case, we infer densities n_H towards the k1-k2 jet of between 10^4 and $3 \times 10^5 \text{ cm}^{-3}$.

Finally, the comparison between the [FeII] 1.64 μm and the H $_2$ 2.12 μm intensities indicates that these emission lines are not spatially correlated, in agreement with the scenario in which [FeII] and H $_2$ are excited by different mechanisms, and the [FeII] emission originates in dissociative shocks. Furthermore, the H $_2$ line intensity clearly increases from the outermost knot to the YSO (see Table 2).

5.2. The outflow driven by the jet

Regarding the mass-loss process, it would be instructive to compare the momentum flux of the atomic jet (\dot{P}_{jet}) with that of the larger-scale CO outflow ($\dot{P}_{\text{CO}} \approx 10^{-5} M_{\odot} \text{ yr}^{-1} \text{ km s}^{-1}$). Unfortunately, the present NIR data do not allow us to measure the momentum flux of the jet directly. By using our derived values of ionisation density (i. e. in the range $6 \times 10^3 - 1 \times 10^4 \text{ cm}^{-3}$) and jet size ($FWHM = 1''.2$), and assuming typical values for the ionisation fraction of 0.03–0.6, and a jet velocity of 100–500 km s^{-1} , we obtained a range of values for \dot{P}_{jet} of $10^{-5}\text{--}10^{-2} M_{\odot} \text{ yr}^{-1} \text{ km s}^{-1}$. The upper limit to this range is clearly unrealistic, which supports a high ionisation fraction, $x_e \geq 0.1$, to limit the jet momentum flux arbitrarily to the more reasonable range of $10^{-5}\text{--}10^{-4} M_{\odot} \text{ yr}^{-1} \text{ km s}^{-1}$ (e.g. Podio et al. 2006). In any case, it appears that $\dot{P}_{\text{jet}} \geq \dot{P}_{\text{CO}}$, which indicates that the [FeII] jet is indeed able to drive the molecular outflow.

6. Summary and conclusions

We have presented our study of the star-forming site located in the globule CB230 using spectroscopic NIR observations. We obtained *JH* and *HK* spectra of the knots in the [FeII] jet, which originates in the low-mass YSO CB230-A, and the protostar itself. This allowed us to derive the physical properties of the region where the jet is launched from. We have also retrieved Spitzer archive data in the range 3.6–70 μm that, complemented with our NIR spectra, enabled us to constrain the relevant physical parameters of the protostar.

Our main results are the following:

1. the spectra of the jet knots show a large number of emission lines, including a rich set of [FeII] lines. The brightest [FeII] and H $_2$ emission lines are spatially uncorrelated, confirming that [FeII] and H $_2$ are excited by different mechanisms, in agreement with the models in which [FeII] traces dissociative J-shocks and molecular hydrogen traces slower C-shocks.
2. the YSO spectrum exhibits a large number of atomic and molecular emission, and absorption features. The characteristics of this spectrum, if photospheric in origin, would correspond to a spectral type later than M2 for CB230-A. They also suggest a lower gravity than for class V stars, which is expected in a protostar where the radius is larger than that of a corresponding main sequence star.
3. complementing flux measurements at different wavelengths with the Spitzer data, we obtained a SED that can be fitted

by a young low-mass ($M < 0.5 M_{\odot}$) protostar with a high (10^{-4} – $10^{-6} M_{\odot} \text{ yr}^{-1}$) accretion rate and a circumstellar disk with $M \leq 0.05 M_{\odot}$. These limits agree with the constraints obtained from the NIR spectrum and the other available mm and sub-mm observations. The occurrence of a cavity of relatively small inclination with respect to the line-of-sight is in accordance with the NIR morphology of the object and explains why a spectrum of the innermost protostellar region has been obtained.

4. as for CB230-B(C), the lack of resolved FIR and sub-mm observations prevented strong constraints by SED fitting being achievable; a large spread in the central mass (0.1 – $1.5 M_{\odot}$) and evolutionary stages (from Class I to Class II) was obtained.
5. the absorption bands of water and CO in the YSO spectrum might be the signature of an active accretion disk, rather than an indication of a photospheric origin. NIR spectra of both high spectral resolution and high signal-to-noise ratio are needed to disentangle the photospheric emission from that of the circumstellar disk, further constraining the protostellar physical parameters.
6. by using intensity ratios involving density-sensitive [FeII] emission lines and following the model by Nisini et al. (2005b), we estimated the electron densities of the [FeII] knots along the jet, obtaining values in the range 6×10^3 – $1 \times 10^4 \text{ cm}^{-3}$.
7. the [FeII] jet appears to be able to drive the larger-scale outflow, exhibiting a higher momentum flux than the CO outflow.

Acknowledgements. This work is based on observations made with the Italian Telescopio Nazionale Galileo (TNG) operated on the island of La Palma by the Centro Galileo Galilei of the INAF (Istituto Nazionale di Astrofisica) at the Spanish Observatorio del Roque de los Muchachos of the Instituto de Astrofísica de Canarias.

This work is based in part on observations made with the Spitzer Space Telescope, which is operated by the Jet Propulsion Laboratory, California Institute of Technology under a contract with NASA.

This publication makes use of data products from the Two Micron All Sky Survey, which is a joint project of the University of Massachusetts and the Infrared Processing and Analysis Center/California Institute of Technology, funded by the National Aeronautics and Space Administration and the National Science Foundation.

This research has also made use of the SIMBAD database, operated at CDS, Strasbourg, France.

We wish to thank F. Palla, L. Testi, F. Bacciotti, L. Podio, A. Isella and A. Natta for helpful discussions and suggestions. We also thank an anonymous referee whose comments helped us to improve the quality of this work.

Appendix A: Estimate of errors due to inaccuracies in the correction of the atmospheric absorption

The effect of an inaccurate correction of atmospheric absorption is assessed as follows. We assume that $T(\lambda, t)$ is the atmospheric transmission at wavelength λ and time t . If the source spectrum $S(\lambda)$ taken at time t_1 is corrected with a T estimated at time t_2 , then the “corrected” spectrum will be:

$$S_{\text{est}}(\lambda) = S(\lambda) \times \frac{T(\lambda, t_1)}{T(\lambda, t_2)} \quad (\text{A.1})$$

The estimated ratio between two lines at wavelengths λ_2 and λ_1 will then be:

$$R_{\text{est}} = \frac{S(\lambda_2) T(\lambda_2, t_1) T(\lambda_1, t_2)}{S(\lambda_1) T(\lambda_2, t_2) T(\lambda_1, t_1)} \quad (\text{A.2})$$

Irrespective of the shape of T , we can then write

$$\frac{T(\lambda_2, t_1)}{T(\lambda_2, t_2)} = \frac{T(\lambda_1, t_1)}{T(\lambda_1, t_2)} + \Delta \quad (\text{A.3})$$

so that Eq. A.2 becomes:

$$R_{\text{est}} = \frac{S(\lambda_2)}{S(\lambda_1)} \left(1 + \Delta / \frac{T(\lambda_1, t_1)}{T(\lambda_1, t_2)}\right) \quad (\text{A.4})$$

or

$$\frac{\Delta R}{R} = \Delta / \frac{T(\lambda_1, t_1)}{T(\lambda_1, t_2)} = A \quad (\text{A.5})$$

The error in the line ratios should then depend only on the ratio of T at a given time to that at a different time.

This ratio can be easily estimated from the ratio of (extracted) spectra of a single object (be it the target or a telluric standard) taken at different times and, obviously, not yet corrected for the atmospheric absorption. We note that this ratio also includes variations due to large-scale sensitivity differences in the detector area and slit misalignments during AB cycles.

As for our observations, we consider spectra of telluric standard stars (HIP97033 and HIP108772), taken both 7 hours before and just prior to the observations of the target. The different ratios of T depend almost linearly on λ in the relevant intervals within the J -, H -, and K -bands, increasing or decreasing with wavelength. The larger slope (in absolute value) is always found in the J -band; it is much smaller for the other bands. We estimated the ratios of T at 1.644, 1.32 and 1.25 μm (JH), and at 2.12 and 1.644 μm (HK). The quantity A derived by using spectra of telluric standards within a same ABBA-cycle (time differences of a few minutes) is almost always ~ 0.1 , or even less. It is likely that, in this case, A is dominated by variations due to large-scale sensitivity differences and slit misalignments during the AB-cycles. When using the target spectra (time differences of a few to 10 minutes), we found again that $A \sim 0.1$. Finally, using telluric standard spectra separated by ~ 7 hrs, we obtained $A \sim 0.8 - 1$ for JH and $A < 0.35$ for HK . By roughly assuming that A increases linearly with time, we again found that $A \sim 0.1$ in JH (much less in HK) within ~ 1 hour, i. e. the maximum time interval between telluric and target observations in JH . Regarding atmospheric absorption, we conclude that line ratios for data acquired using a same grism should be accurate to within 10%, after taking account of both variations due to large-scale sensitivity differences and slit misalignments during AB-cycles.

Problems arise only in observed wavelength ranges affected by the strong telluric absorption between the J -, H - and K -bands, which correspond to the edges of the three bands. In this respect, the changes in slopes occurring at wavelengths close to the edges of the three segments of spectrum (where the noise also increases) have to be regarded with caution. They might have been increased by variations of telluric absorption that have been unaccounted for.

Appendix B: Reliability of the [FeII] 1.645/1.257 μm line ratio as an extinction estimator

As stated in the text, the [FeII] line ratios 1.645/1.321 μm and 1.645/1.257 μm can be used to estimate the extinction towards the [FeII]-emitting regions, since all of these lines originate in the same upper energy level. However, Nisini et al. (2005b) found that the 1.645/1.257-ratio systematically underestimates

the extinction towards a number of sources. They suggested that this may be due to a poor determination of the Einstein coefficients. This can be checked easily because any discrepancies in the adopted Einstein coefficients should produce a fixed systematic difference between the values of A_V determined from the two line ratios for any observational dataset. If this difference was then found not to be constant (within errors), alternative sources of contamination should be considered.

Such a check is beyond the scope of this paper. We propose another possibility that does not involve the Einstein coefficients; the cause would be the same as that envisioned by Bailey et al. (2007), i. e. an error in the atmospheric correction occurring in low (and possibly also mid) spectral-resolution spectra, in this case affecting the $1.257 \mu\text{m}$ line. This line is in a wavelength range containing the $^1\Delta_g$ absorption band of O_2 . At high spectral resolution, Fig. 8 of Bailey et al. (2007) shows that there are many narrow lines that lower the transmission to almost zero at their central wavelengths, in the same region in which the $1.257 \mu\text{m}$ line is located. At low resolution, these high-opacity absorption lines are smoothed away and produce a broad depression in the empirically-obtained atmospheric transmission curve. If the observed wavelength range of the [FeII] line corresponded to one of the narrow, atmospheric absorption lines, it would be underestimated following telluric correction. This would lead to an overestimate of the $1.645/1.257$ -ratio and, in turn, to an overestimate of the extinction when this was derived from the ratio, the situation which has indeed been found. It is difficult to assess the magnitude of the error without a detailed modelling of both the atmospheric absorption and the [FeII] line.

References

- Allen, L. E., Calvet, N., D'Alessio, P., et al. 2004, *ApJS*, 154, 363
 Allers, K. N., Jaffe, D. T., Luhman, K. L., et al. 2007, *ApJ*, 657, 511
 André, P., Ward-Thompson, D., & Barsony, M. 2000, *From Protostellar Cores to Protostars: the Initial Conditions of Star Formation*, in *Protostars and Planets IV*, ed. V. Mannings, A. P. Boss, & S. S. Russell (Tucson: Univ. Arizona Press), 59
 Bacciotti, F., & Eisloffel, J. 1999, *A&A*, 342, 717
 Bailey, J., Simpson, A., & Crisp, D. 2007, *PASP*, 119, 228
 Bok, B. J., & Reilly, E. F. 1947, *ApJ*, 105, 255
 Brand, J., Wouterloot, J. G. A., Codella, C., & Massi, F. 2008, in preparation
 Calvet, N., Hartmann, L., & Kenyon, S. J. 1991a, *ApJ*, 383, 752
 Calvet, N., Patino, A., Magris, G. C., & D'Alessio, P. 1991b, *ApJ*, 380, 617
 Chen, X., Launhardt, R., & Henning, T. 2007, *ApJ*, 669, 1058
 Clemens, D. P., & Barvainis, R. 1988, *ApJS*, 68, 257
 Codella, C., Brand, J., Massi, F., Wouterloot, J. G. A., & Davis, G. R. 2006, *A&A*, 457, 891
 Cushing, M. C., Rayner, J. T., & Vacca, W. D. 2005, *ApJ*, 623, 1115
 Dallier, R., Boisson, C., & Joly, M. 1996, *ApJS*, 116, 239
 Doppmann, G. W., Greene, T. P., Covey, K. R., & Lada, C. J. 2005, *AJ*, 130, 1145
 Froebrich, D. 2005, *ApJS*, 156, 169
 Fazio, G. G., Hora, J. L., Allen, L. E., et al. 2004, *ApJ*, 154, 10
 Gordon, K. D., Engelbracht, C. W., Fadda, D., et al. 2007, *PASP*, 119, 1019
 Huard, T. L., Sandell, G., & Weintraub, D. A. 1999, *ApJ*, 526, 833
 Kun M. 1998, *ApJS* 115, 59
 Lancon, A., & Rocca-Volmerange, B. 1992, *A&AS*, 96, 593
 Lancon, A., & Wood, P. R. 2000, *A&AS*, 146, 217
 Launhardt, R., & Henning, Th. 1997, *A&A*, 326, 329
 Launhardt, R. 2001, *Fragmentation of a Protostellar Core: The Case of CB 230*, in *The Formation of Binary Stars*, ed. H. Zinnecker, & R. D. Mathieu, *Proceedings of IAU Symp.* 200, 117
 Leggett, S. K., Allard, F., Dahn, C., et al. 2000, *ApJ*, 535, 965
 Leggett, S. K., Allard, F., Geballe, T. R., Hauschildt, P. H., & Schweitzer, A. 2001, *ApJ*, 548, 908
 Maillard, J. P., Chauville, J., & Mantz, A. W. 1976, *J. of Molec. Spectr.*, 63, 120
 Maiolino, R., Rieke, G. H., & Rieke, M. J. 1996, *AJ*, 111, 537
 Massi, F., Codella, C., & Brand, J. 2004, *A&A*, 419, 241
 McGovern, M. R., Kirkpatrick, J. D., McLean, I. S., et al. 2004, *ApJ*, 600, 1020
 McLean, I. S., McGovern, M. R., Burgasser, A. J., et al. 2003, *ApJ*, 596, 561
 Meyer, M. R., Edwards, S., Hinkle, K. H., & Strom S. E. 1998, *ApJ*, 508, 397
 Mould, J. R., Hall, D. N. B., Ridgway, S. T., Hintzen, P., & Aaronson, M. 1978, *ApJ*, 222, L123
 Muzerolle, J., Hartmann, L., & Calvet, N. 1998, *AJ*, 116, 2965
 Nisini, B., Antonucci, S., Giannini, T., & Lorenzetti, D. 2005a, *A&A*, 429, 543
 Nisini, B., Bacciotti, F., Giannini, T., et al. 2005b, *A&A*, 441, 159
 Origlia, L., Moorwood, A. F. M., & Oliva, E. 1993, *A&A*, 280, 536
 Palla, F., & Stahler, S. W. 1991, *ApJ*, 375, 288
 Palla, F., & Stahler, S. W. 1992, *ApJ*, 392, 667
 Palla, F., & Stahler, S. W. 1993, *ApJ*, 418, 414
 Podio, L., Bacciotti, F., Nisini, B., et al. 2006, *A&A*, 456, 189
 Reid, I. N., Burgasser, A. J., Cruz, K. L., Kirkpatrick, J. D., & Gizis, J. E. 2001, *AJ*, 121, 1710
 Reach, W. T., Megeath, S. T., Cohen, M., et al. 2005, *PASP*, 117, 978
 Rieke, G. H., & Lebofsky, M. J. 1985, *ApJ*, 288, 618
 Rieke, G. H., Young, E. T., Engelbracht, C. W., et al. 2004, *ApJS*, 154, 25
 Robitaille, T. P., Whitney, B. A., Indebetouw, R., Wood, K., & Denzmore, P. 2006, *ApJS*, 167, 256
 Robitaille, T. P., Whitney, B. A., Indebetouw, R., & Wood, K. 2007, *ApJS*, 169, 328
 Shu, F. H., Najita, J. R., Shang, H., & Li, Z.-Y. 2000, *X-Winds Theory and Observations, in Protostar and Planets IV*, ed. V. Mannings, A. P. Boss, & S. S. Russel (Tucson: University of Arizona Press), 789
 Siess, L., Dufour, E., & Forestini, M. 2000, *A&A*, 358, 593
 Straizys, V., Cernis, K., Kazlauskas, A., & Meistas, E. 1992, *Baltic Astr.*, 1, 149
 Wallace, L., Meyer, M. R., Hinkle, K., & Edwards, S. 2000, *ApJ*, 535, 325
 Whitney, B. A., & Hartmann, L. 1993, *ApJ*, 402, 605
 Whitney, B. A., Kenyon, S. J., & Gómez, M. 1997, *ApJ*, 485, 703
 Wuchterl, G., & Tscharnuter, W. M. 2003, *A&A*, 398, 1081
 Young, C. H., Shirley, Y. L., Evans, N. J. II, & Rawlings, J. M. C. 2003, *ApJS*, 145, 111
 Young, C. H., Bourke, T. L., Young, K. E., et al. 2006, *AJ*, 132, 1998
 Yun, J. L., & Clemens, D. P. 1992, *ApJ*, 385, L21
 Yun, J. L., & Clemens, D. P. 1994a, *ApJS*, 92, 145
 Yun, J. L., & Clemens, D. P. 1994b, *AJ*, 108, 612